HHS Public Access

Author manuscript

Nat Biomed Eng. Author manuscript; available in PMC 2022 October 24.

Published in final edited form as:

Nat Biomed Eng. 2022 October ; 6(10): 1167–1179. doi:10.1038/s41551-021-00810-0.

Enhanced tendon healing by a tough hydrogel with an adhesive side and high drug-loading capacity

Benjamin R. Freedman[1,2], **Andreas Kuttler**[3], **Nicolau Beckmann**[3], **Sungmin Nam**[1,2], **Daniel Kent**[2], **Michael Schuleit**[3], **Farshad Ramazani**[3], **Nathalie Accart**[3], **Anna Rock**[2], **Jianyu Li**[4], **Markus Kurz**[3], **Andreas Fisch**[3], **Thomas Ullrich**[3], **Michael W Hast**[5], **Yann Tinguely**[2], **Eckhard Weber**[3,*], **David J. Mooney**[1,2,*]

[1]John A. Paulson School of Engineering and Applied Sciences, Harvard University, Cambridge, MA, USA, 02139

[2]Wyss Institute for Biologically Inspired Engineering, Harvard University, Boston, MA, USA, 02115

[3]Novartis Institutes for Biomedical Research, Basel, Switzerland, 4033

[4]Department of Mechanical Engineering, McGill University, Montreal, CA, H3A 2T5

[5]Biedermann Lab for Orthopaedic Research, Department of Orthopaedic Surgery, University of Pennsylvania, Philadelphia, PA, USA, 19104

Abstract

Hydrogels that provide mechanical support and sustainedly release therapeutics have been used to treat tendon injuries. However, most hydrogels are insufficiently tough, release drugs in bursts, and require cell infiltration or suturing to integrate with surrounding tissue. Here, we report that a hydrogel serving as a high-capacity drug depot and combining a dissipative tough matrix on one side and a chitosan adhesive surface on the other side supports tendon gliding and strong adhesion (larger than 1,000 J/m2) to tendon on opposite surfaces of the hydrogel, as we show with porcine and human tendon preparations during cyclic-friction loadings. The hydrogel is biocompatible, strongly adheres to patellar, supraspinatus and Achilles tendons of live rats, boosted healing and reduced scar formation in a rat model of Achilles-tendon rupture, and sustainedly released the corticosteroid triamcinolone acetonide in a rat model of patellar tendon injury, reducing inflammation, modulating chemokine secretion, recruiting tendon stem and progenitor cells, and promoting macrophage polarization to the M2 phenotype. Hydrogels with ‘Janus’ surfaces and sustained-drug-release functionality could be designed for a range of biomedical applications.

Correspondence and requests for materials should be addressed to E.W. or D.J.M., mooneyd@seas.harvard.edu, eckhard.weber@novartis.com. * Co-corresponding Authors.

Author contributions

All authors contributed to the preparation of this manuscript. B.R.F., A.K., S.N., D.K., S.N., A.R., N.B., and E.W. performed the experiments. B.R.F., A.K., N.B., and Y.T. performed data analysis. B.R.F., E.W., and D.J.M. planned experiments.

Peer review information *Nature Biomedical Engineering* thanks Manuela Gomes, Stavros Thomopoulos and Xuanhe Zhao for their contribution to the peer review of this work. Peer reviewer reports are available.

Tendon injuries throughout the human body are common, and often accompanied by tissue inflammation and degeneration; these injuries are also recognized complications following bone fracture fixation[1–5]. Although many new surgical, rehabilitation, graft, and drug therapeutics have been proposed[6–10], with some taken to market[10–12], failed tendon healing and persistent pain remain significant unmet medical needs. New biomaterial-based therapies may address these unmet needs by providing mechanical support and effective spatial and temporal targeted delivery of drug therapeutics to tendon tissue[13,14]. Use of hydrogels may be particularly appealing due to their general biocompatibility with surrounding tissues, the tunability of their physical properties, and their ability to serve as a depot for drug delivery. However, hydrogels typically exhibit poor mechanical toughness and adhesive properties, and rely on cell infiltration or suturing to integrate with surrounding tissue, and frequently exhibit burst release of drugs[15].

To promote tendon healing via mechanical support and local delivery of drug therapeutics, hydrogels should be placed and remain near the relevant anatomical site. If used for spatial and temporal targeted delivery of therapeutics, hydrogels are considered to reduce potential systemic toxicity and side effects[16] commonly associated to orally delivered medications such as NSAIDs[17–20] and promote local drug retention and extended dosing intervals following injection of drugs such as corticosteroids[21 22–24]. However, physical distortion by movement following injection or implantation of hydrogels can lead to displacement and mechanical fragmentation[10,25]. Adhesion of hydrogels to tissue was suggested to circumvent some of the limitations of classical hydrogels[26]. Adhesive hydrogels may facilitate the diffusion of a drug from the hydrogel drug depot to the target tissue rather than to the surrounding tissue by increasing the direct contact surface and by reducing the diffusion barrier. Adhesive hydrogels may thus offer an intriguing concept for locally restricted and sustained drug delivery system for the therapy of tendon injuries. Tissue adhesives approved for medical use such as fibrin glues (TISSEEL) and cross-linked polyethylene glycols (COSEAL) may be used as adhesive hydrogels, but their adhesive strength is low[26]. Cyanoacrylates (Dermabond) are tissue adhesives with high mechanical strength[27], however they are cytotoxic to tendon derived cells[28], incompatible with wet tissue surfaces[26], may chemically react with encapsulated drugs during setting, and form rigid connections upon contact with water[26]. The importance of augmenting tendon gliding following repair has prompted active research, as a common limitation of healing is fibrotic scar formation, presumably caused by high friction between the healing tendon and surrounding tissues[29,30]. Furthermore, to protect tendons from tendon injury following bone fracture fixation (e.g., volar plate fixation of distal radius fractures[31,32]), adhesive hydrogels should also support tendon gliding[33–35].

Here we describe a tough adhesive hydrogel, termed Janus Tough Adhesive (JTA), with tissue adherent versus tissue gliding properties on opposing surfaces to serve as a high-capacity depot for drug delivery to tendon (Fig. 1). High mechanical toughness of the JTA was achieved using a dual interpenetrating hydrogel network that combines the ability of alginate hydrogels to dissipate energy through dissociation of ionic bonds with a highly elastic covalently cross-linked acrylamide hydrogel that can distribute stresses throughout the network[36,37]. Adhesion to tissue was achieved by unilateral coupling of the amine rich bridging polymer chitosan to the dissipative alginate acrylamide hydrogel[26]. It was

hypothesized that the JTA would simultaneously provide mechanical tissue integrity and controlled spatial and temporal drug delivery for the treatment or prevention of tendon injury.

Results

JTA adheres strongly to tendons while simultaneously supporting tissue gliding ex vivo.

The adhesion strength of the JTA to tendon was first investigated. Bovine tendon samples were prepared by cutting tissues into thin tendon planks using a cryotome (Fig. 2a). After applying the positively charged bridging polymer chitosan to one surface of the tough dissipative alginate acrylamide hydrogel (Fig. 2b) and bringing this surface into contact with tendon, the chitosan diffused into the tough hydrogel and tendon surfaces rapidly (Fig. 2c,d) and generated strong adhesion (Fig. 2e; Supplementary Movie 1). The adhesion energy increased over time, exceeding the fibrin glue TISSEEL within one minute of application (Fig. 2f). Adhesion energy in the swollen state after 24h incubation in DMEM at 37°C was not significantly different than pre-swelling (Supplementary Fig. 1; Supplementary Movie 2).

As a step towards translational application to anatomically larger tendons, the versatility of the JTA was explored in a porcine *in situ* model. The JTA adhered strongly to porcine patellar tendon, flexor tendon, and Achilles tendon (Fig. 2g,h) even in the presence of blood (Supplementary Movies 3–5). Adhesion was generated rapidly, and the JTA conformed well to tissue surfaces. The JTA demonstrated superior adhesion energy to tendon in bloody environments, as may be present during orthopaedic surgeries, compared to cyanoacrylate (Dermabond) and hemostatic mesh (SurgiCel) (Figs. 2i,j; Supplementary Fig.2; Supplementary Movie 3).

Because the JTA was adherent to tissue on only one side, we tested the ability of the opposite non-adherent side of the JTA to support tendon gliding. Friction testing revealed that the non-adherent surface demonstrated very low coefficients of friction (μ_k) when in contact with adjacent tissue, even below the value of tissue on tissue contact over hundreds of cyclic loadings that mimic *in vivo* loading (Fig. 3a–d; Supplementary Movie 6). In tendon-tendon friction tests, damage to the epitenon was present by the end of the test, unlike JTA-tendon groups. The ability of the JTA to support gliding was next examined in human cadaveric wrists in situ when used as a protective barrier over the flexor pollicis longus (Fig. 3e; Supplementary Fig.3a,b). Here, the JTA withstood friction as it glided over the volar plate and passed through the transverse carpal ligaments. The JTA adhered well to the flexor pollicis longus and withstood gliding over the volar plate into the transverse carpal ligaments (Supplementary Fig.3c; Supplementary Movie 7).

JTA is biocompatible and promotes tendon healing.

To evaluate the performance of the JTA *in vivo*, rats with full thickness, partial width excisional injuries made to the central midsubstance of their patellar tendons, or left uninjured, were either treated with the JTA or left untreated (Fig. 4a). The thickness of the JTA was assessed to evaluate any potential swelling or degradation applying serial high

frequency ultrasound imaging (Fig. 4b; Supplementary Movie 8). No changes were observed in JTA thickness over the 3-week observation period.

After 3-weeks, the patellar tendons were harvested, imaged axially using ultrasound, and prepared for mechanical testing or used for histology (Supplementary Fig.4; 5a). Tendon injury, but not application of the JTA, increased tendon cross sectional area (Supplementary Fig.5b). Also, injury decreased tendon echogenicity, indicative of reduced collagen packing or organization (Fig. 4d)[38]. The JTA improved impaired relaxation of injured tendons (Fig. 4c), but did not affect the elastic tendon mechanics, dynamic modulus (Fig. 4e) and linear modulus of naive and injured tendons. Tendon injury, as expected, impacted these elastic properties of tendon mechanics (Supplementary Fig.5d). The toe modulus, percent relaxation, and tan(δ) were not affected by JTA or injury (Supplementary Fig.5c,e,f). In agreement with mechanical data, injury, but not JTA implantation, was found to affect the tendon cellularity and shape (Fig. 4g,h).

Unlike the patellar tendon, the rotator cuff presents additional adhesive attachment challenges, but remains a primary type of tendon injury requiring surgical intervention[39]. Mechanical support of the bone-tendon interface (i.e., enthesis) is critical to support healing of rotator cuff tendon injury. Because tendon and bone differ greatly in composition, structure, and mechanics, the periosteal surface of bone was first assessed *ex vivo* for adhesion of the JTA (Supplementary Fig.6a,b; Supplementary Movie 9). An *in vivo* study was thus conducted in a rat rotator cuff model[40] to evaluate adhesion of JTA to the enthesis of both naive and injured supraspinatus tendon following partial tenotomy (Fig. 4i; Supplementary Fig.6c). Here, the footprint of the JTA was expanded to cover the enthesis and pass under the acromion for additional structural support. Following implantation, serial magnetic resonance imaging (MRI) was applied to evaluate the anatomical position of the JTA over time and to assess inflammatory tissue response to the JTA (T2-weighted images). MRI analysis confirmed that placement of the JTA was maintained throughout the duration of the study as animals resumed cage activity (Fig. 4j). MRI and subsequent tissue histology also demonstrated the lack of overt tissue inflammation in response to JTA implantation (Supplementary Fig.6d,e). Surgery and JTA implantation had a minimal, non-significant impact on the animal body weights (Supplementary Fig.7). Results suggest that the JTA is well tolerated following implantation in the anatomically and functionally complex rotator cuff compartment.

To examine whether the JTA could augment tendon repair, the effect of tendon repair with and without JTA implantation was investigated in an Achilles tendon rupture model (Fig. 4k). JTAs remained in place over the injury site throughout the duration of their 3-week implantation (Fig. 4l; Supplementary Fig.8a) and resulted in a 25% reduction in tissue formation compared to repaired only treatment (Fig. 4m). However, no differences in the dynamic modulus or tanδ at 4% strain were detected (Supplementary Fig.8b,c).

The biocompatibility of the JTA was further confirmed *in vitro* by placing tendon derived cells in contact with the JTA; cells maintained high viability (>95%) following incubation with JTA (Supplementary Fig.9).

JTA enables high drug loading and sustained drug release in silico and in vitro.

The delivery of the corticosteroid, triamcinolone acetonide (CORT)[41], was used as a model drug to examine drug loading and release from the JTA. First, the diffusion of CORT through the JTA was examined using a Franz cell (Fig. 5a). The JTA substantially slowed diffusion of CORT compared to the JTA-supporting PVDF membrane only (Fig. 5b). Computational modeling was used to calculate the diffusion constant of CORT through the JTA ($D=16\ \mu m^2/s$), which was substantially lower than that through a PVDF membrane ($D=305\ \mu m^2/s$)[42]. The tough hydrogels were loaded up to 25000x the solubility limit of CORT[43] (Fig. 5c). Drug loading was accomplished by adding a CORT microcrystal suspension to the high viscosity alginate acrylamide hydrogel prior to crosslinking. Although the CORT was micronized (Supplementary Fig.10a), the particles formed larger aggregates in the JTA at high loading (size $>150\mu m^2$) (Fig. 5d; Supplementary Fig.10b). The addition of CORT turned the color of the JTA from clear to white (Supplementary Fig.10c). Finite element (FE) simulations were performed to model the release of CORT from the JTA under well mixed conditions (Fig. 5e). As expected, the model predicted sequential dissolution of drug particles in turn starting from the periphery, leading to a sustained dissolution-controlled CORT release from the system (Fig. 5e–g; Supplementary Movie 10). The model predictions agreed with experimental observation of release from JTA, with drug release extending for 2–10 days in a manner dependent on the initial CORT loading (Fig. 5h). Notably, the JTA loaded with CORT at 4-times the polymer content (500mg/ml) still maintained its mechanical and adhesive properties (Fig. 5j,i; Supplementary Fig.10d). Regardless of CORT loading, the viability of tendon derived cells exposed to CORT-loaded JTA remained high *in vitro* (Supplementary Fig.11d).

JTA adherent to tendon provides sustained CORT release in vivo.

To investigate whether CORT-loaded JTA could provide sustained release *in vivo*, studies in the rat model of patellar tendon injury were conducted (Fig. 6a; Supplementary Fig.8). Serial in-life high frequency ultrasound (HFUS) analysis revealed that the JTA remained in place adjacent to the patellar tendon for at least two weeks (Fig. 6c, Supplementary Fig.12a; Supplementary Movie 11), and maintained placement was confirmed by histology post-mortem (Supplementary Fig.12b). Quantification of CORT in serum confirmed that the sustained release observed *in vitro* also occurred through one-week *in vivo* (Fig. 6b). Next, a depot JTA system was utilized in which the cylindrical interior depot maintained a high CORT concentration (100mg/ml), flanked and topped by a blank hydrogel (Supplementary Fig.9a). The blank JTA cover was used to further support a smaller JTA containing CORT that effectively reduced the net dose of CORT while maintaining a high drug loading and adhesion to tendon (Fig. 6j; Extended Data Fig.1). The high drug loading resulted in extended drug dissolution time and drug release. The JTA was also well tolerated in the rat patellar tendon model *in vivo* (Extended Data Fig.1b,c). JTA+CORT significantly decreased endogenous corticosterone levels in serum at day 2 post-implantation (Extended Data Fig.1d). JTA and JTA+CORT had immune modulatory effects and significantly decreased the serum chemokine GRO-α at day 2 post–injury (Extended Data Fig.2a). JTA+CORT also increased the serum chemokine RANTES at day 14 post-injury (Extended Data Fig.2b) The JTA itself reduced the level of vascularity, in early healing, and JTA+CORT further reduced vascularity at day 3 post-implantation (Fig. 6d,e; Supplementary Movie 12).

Two-weeks post injury, patellar tendons were harvested and evaluated for their morphology, echogenicity, and biomechanical properties (viscoelastic, dynamic, and quasi-static). Injured tendons had decreased echogenicity and elevated mechanical relaxation compared to uninjured tendons (Fig. 6f,g). In contrast, injured patellar tendons receiving JTA or JTA+CORT were not statistically different than uninjured tendons (Fig. 6f,g). As expected, injury decreased the dynamic modulus regardless of JTA implantation or CORT delivery (Fig. 6h).

Full length images were acquired of the patellar tendon to carefully isolate the midstance with (Fig. 7a) or without (Fig. 7b) injury. Tendon injury significantly increased tendon cellularity, which was further elevated in groups receiving JTA+CORT (Fig. 7c). JTA+CORT had immune modulatory effects as demonstrated by elevation of CD68 (macrophage) positive staining (Fig. 7d), which is indicative for the M2 macrophage reparative phenotype (Arg-1) (Fig. 7e). JTA alone elevated the proportion of CD146 positive cells (tendon stem/progenitor) (Extended Data Fig.3d), but had no effect on CD45 (non-specific immune cell), CD31 (endothelial cell), αSMA (myofibroblast), or iNOS (M1 macrophage) staining (Extended Data Fig.3b,c,e,f). JTA and JTA+CORT had no effect on the injury-decreased nuclear aspect ratio and second harmonic generation (SHG) signal at week 2 post-injury (Extended Data Fig.3a; 7f).

Discussion

This study engineered and characterized a JTA for the treatment and prevention of recurrence of tendon injury. Although many hydrogel-based materials are used in wound dressings, tissue repair and regeneration, medical implants, transdermal drug delivery, and bioelectronics[44], none exhibit appropriate adhesive properties and the broad versatility necessary for tendon applications. In addition to investigating its adhesive properties *in vitro*, the JTA was tested in multiple tendon models *in situ* and *in vivo*, highlighting the broad utility of the JTA and its potential advantages when used as a mechanical support and delivery system of drug therapeutics.

Although there is no FDA approved adhesive for tendon repair, TISSEEL has been suggested for potential clinical use in tendon[45]. The JTA interacts well with wet tendon surfaces and exhibits a ~16-fold increase in adhesion energy, as compared to the fibrin glue, TISSEEL. This strong adhesion may be attributed to the multicomponent adhesion mechanisms and high toughness not present in adhesive hydrogels in current clinical use[26]. The high toughness of the JTA likely plays an integral role in avoiding cohesive failure and dissipating energy at the adhesive interface to ensure strong adhesion to tendon and provide mechanical support. Notably, without application of the bridging polymer, the JTA was immediately displaced upon closure of the skin. Although other hydrogels may also exhibit low coefficients of friction, the high mechanical toughness of the JTA enables its mechanical integrity following *in vivo* loading. Most hydrogels (e.g., single network) are too brittle to carry out this level of performance. The tough hydrogel double network has mechanical toughness beyond native tissue.[37] In contrast, naturally derived extracellular matrix (GraftJacket) and small intestine submucosa (CuffPatch), and synthetic variants (Artelon) used clinically to provide mechanical support for tendon repair do not adhere

strongly to tissue[10]. In vivo studies show that the JTA remains adjacent to the Achilles tendon, patellar tendon, and rotator cuff tendons for at least 3 weeks, and future studies will examine even longer time points. The current design of the JTA is not intended to mimic or replace native tendon tissue, but to inspire and promote natural tendon healing. The JTA shall serve as a strong adhesive to tendon for local extended drug delivery and shall augment tendon gliding. Future work will explore strategies to add further mechanical functionality to the JTA (e.g., mechanical properties mimicking native tendons to serve as an adhesive reinforcement material).

The importance of augmenting tendon gliding following repair has prompted active research, as a common limitation of healing is fibrotic scar formation, presumably caused by high friction between the healing tendon and surrounding tissues[29,30]. Notably, the non-chitosan coated side of the tough adhesive supported gliding at lower friction than normal tendon on tendon. This ability to promote gliding with surrounding tissue could improve joint range of motion and accelerate return to activity, and its functional importance and potential therapeutic impact will be further examined in future studies. Here we demonstrate this property of the JTA with various animal and human tendons, supporting its broad relevance to numerous types of tendon injuries. Further, the low friction and tunable mechanical properties of the JTA is likely relevant for other orthopaedic applications with tissues requiring gliding, including cartilage, meniscus, and muscle. Future work is needed to determine friction performance for thousands of cycles in vivo over time.

It is well established that tendons heal through scar formation and exhibit long term structural, compositional, and material property deficits due to scarring[46–50]. Indeed, two FDA approved technologies [VersaWrap (Alafair Biosciences) and Tenoglide (Integra LifeSciences)] are indicated for the protection and management and protection of tendon injuries in which there has been no substantial loss of tendon tissue, by keeping damaged tissues physically separated during healing. The potential for reduced tissue CSA shown with JTA treatment following Achilles tendon repair suggests promise of this approach and requires further evaluation including long term beneficial effects of the JTA on mechanical tendon function. Although neither the JTA nor standard of care alone restored viscoelastic properties in the complete Achilles tendon transection model, past studies demonstrated improvement in viscoelastic properties, indicative for compositional properties of tendon remodeling, only in a later phase of tendon healing[51,52].

Local delivery often requires placement or suturing of drug delivery depots[53] near the tissue of interest, but this approach may suffer from depot migration and depot disintegration over time due to dynamic tissue movement[10,25]. The JTA design is appealing since its adhesive properties prevent migration over time and its high toughness makes it resistant to mechanical disintegration due to tissue movement. The adhesive drug depot concept and design is highly versatile and may also enable other drug delivery systems to be easily integrated and stabilized, while providing additional control over release. Further, while many drug depot systems suffer limited loading capacities (0.01–1mg/ml) and frequently exhibit burst release of a large fraction of the loaded drug[15], the JTA is capable of drug loading over 4-times its polymer content (up to 500mg/ml), and release over 10 days under perfect sink conditions *in vitro* and over 1-week *in vivo*. Ongoing work is examining

additional strategies to extend release, such as the model drug, triamcinolone acetonide encapsulated in nanoparticles that are then encapsulated in the JTA, and role of adhesion in modulating release into target tissues.

Both computational and experimental models confirmed that the release of triamcinolone acetonide was controlled by dissolution. Additionally, the JTA itself was found to hinder diffusion of the small-sized chemical triamcinolone acetonide, possibly due to the extremely low mesh size of the tough hydrogel[54]. This low diffusion is similar to that reported in certain other hydrogels such as contact lenses[55]. The dissolution-controlled release of triamcinolone acetonide from the JTA examined here suggests that this strategy may be effective for other hydrophobic drug therapeutics as well. Future studies will examine the capacity of the JTA to serve as delivery system for biomolecules and cells locally to tendon (e.g., through integrating cell laden scaffolds or adhering of cells to the surface of the JTA).

While triamcinolone acetonide was used in the current work as a model drug, the use of corticosteroids to mitigate pain and inflammation on tendon has been controversial for decades[23,24,56–58]. Although some studies suggest potentially harmful effects of corticosteroids on tendon health, e.g. decreased tissue viability[59,60], increased apoptosis[59], loss of fibroblastic appearance[61], decreased expression of collagen-I[61], those studies tended to utilize *in vitro* tissue culture models with concentrations 20–200x higher than applied in the present study. Lower tendon tissue concentrations of corticosteroids may not be detrimetnal[22,62] and in contrast it was suggested that sustained release may improve tendon biomechanics[58].

The JTA with or without triamcinolone acetonide (CORT) modulated immune responses to tendon injury and provided early signals for potential improvement of tendon healing. Following JTA and JTA+CORT treatment, cellularity and M2 macrophage polarization was increased, the latter suggested by the increase in Arg1 immuno-positive CD68 expressing cells. The mechanism of M2 macrophage polarization remains however ambiguous, because chitosan present in the adhesive layer of the JTA has been shown to induced M2 polarization[63–67], similar to triamcinolone acetonide alone[68,69]. In the present study, the pharmacodynamic activity of triamcinolone acetonide following release from the JTA was demonstrated by the feedback-inhibition of endogenous corticosterone levels at day 2 post-implantation, which occurred in concert with a decrease in serum GROα levels, a chemokine affecting recruitment and activation of neutrophils. In addition to signal marker indicating modulation of immune responses by JTA and/or triamcinolone acetonide, the increased number of CD146 positive cells, a marker for tendon/stem progenitor cells[70,71], represents a signal for tendon regeneration and thus for putative improvement of tendon healing. These early signal markers for putative improvement of tendon healing at 2 weeks post-injury require validation in subsequent more chronic studies, in which JTA will be evaluated to promote sustained improvement of biomechanical tendon function.

An appealing translational feature of the JTAs is that most components are approved for use by the FDA in other devices and are widely used for other clinical applications. Alginate, chitosan, and polyacrylamide are used in several commercialized products and have undergone extensive animal testing for internal and external indications[26,72,73]. Alginate

and chitosan have been used in many wound dressings (e.g., Algisite M, ChitoFlex) and as systems for protein delivery (e.g., Emdogain[74–76]), and polyacrylamide (e.g., Bulkamid) is used as a filler material in treatment of urinary incontinence[77,78]. These favorable properties of the materials together with the demonstrated scalability to larger tissues position the JTA for further development for clinical applications. Given the mechanical performance, gliding features, and drug delivery concept of the JTA, the most relevant clinical uses include the promotion of gliding through adjacent structures and local release of small molecules. The JTA itself is likely to be regulated as a class II device (510(k)), whereas translation of the drug delivering JTA will likely be regulated as a class III PMA combination product. Additional clinical uses may be possible but were not investigated in the present study. Taken together, the design of JTA for the treatment and prevention of recurrence tendon injury described here may enable a range of applications, such as the potential augmentation of sutures, the simultaneous promotion of mechanical support and tendon gliding, and the local delivery of drugs.

Methods

Janus Tough Adhesive Synthesis.

Tough gels were synthesized by mixing one syringe containing a 10ml solution of 2% sodium alginate [combining a high (MW=200kDa) and low (MW=30kDa) molecular weight alginate at 1:1 ratio; MVG or LF20/40 and VLVG or LF 20/40 irradiated, (Pronova, Novamatrix Norway)] and 12% acrylamide (Sigma, A8887) in HBSS (Gibco), 36μl of 2% N,N'-methylenebis(acrylamide) (Sigma, M7279), and 8μl of TEMED (Sigma, T7024), with a second syringe containing 226μl of 6.6% ammonium persulfate (Sigma, A9164), and 191μl of 0.75M calcium sulfate dihydrate (Sigma, 31221). The gel was cast into molds ($80\times15\times1.5mm^3$) sealed on both sides with glass and left to crosslink for 24h. After 24h, tough gel strips were removed from molds and stored in sealed plastic bags at 4°C.

To form the JTA, UP chitosan (2%) (UP Chitosan 54046, Heppe Medical Chitosan, Halle, Germany) and coupling reagents (1-ethyl-3-(3-dimethylaminopropyl) carbodiimide (Sigma, E6383) and sulfated N-hydroxy-succinimide) (Thermofisher, PG82071) (12mg/ml) were quickly mixed by vortexing. This mixture was applied to the surface of the tough gel (25μl/cm^2) and compressed to the tissue surface.

Adhesion Energy Application and Measurement.

Thin tendon planks ($15\times1\times40mm^3$) were prepared from bovine flexor tendons using a freezing stage microtome (CM1950, Leica, Wetzlar, Germany). Tough hydrogel strips were synthesized and thin 0.003mil PET backing layers were placed adjacent to the strips and attached with superglue (Loctite 454). The end of the tough hydrogel-PET composite was secured with thin acrylic pieces ($2\times1cm^2$) and superglue. The tough hydrogel was then adhered to tendon planks as described above while sandwiched under strain control between glass slides[26]. Adhesion energy was measured with 180° peeling tests (Instron 3342, Norwood, MA) under uniaxial tension (100mm/min). Using captured force and displacement data, the adhesion energy was quantified by multiplying the steady state force

by two and dividing by the sample width. Commercially available fibrin sealant (TISSEEL, Baxter) was tested in a similar manner as a control.

The effect of JTA swelling after incubation in DMEM was investigated. Tendon samples were adhered to the JTA and maintained in DMEM at 37°C for 24h. After 24h, samples were peel tested using the same methods as described.

90-degree peel adhesion tests were completed in fresh cadaver tendons (Movie S6). Adhesion strength after 10 minutes of application was not significantly different to tendon plank testing (Fig. 2h).

Interpenetration of Bridging Polymer.

Interpenetration of the bridging polymer into the tissue was assessed using FITC-labeled chitosan[79] and confocal microscopy (LSM710, Zeiss, Oberkochen, Germany). Thin tendon samples were created using a cryotome and biopsy punched into discs (diameter 8mm, thickness 1mm). Tough gel discs (diameter 8mm, thickness 1mm) were synthesized. Using a similar application process as above, the JTA was applied to tendon surfaces with the FITC-labeled chitosan and evaluated for interpenetration into tendon tissue after 1, 10, and 100 minutes. At these timepoints, the tendon-JTA composite was snap frozen in liquid nitrogen, bisected, and cryosectioned (section thickness = 40μm). Sections were then stained with DAPI and mounted (Prolong™ Gold Antifade Mountant with DAPI, ThermoFisher). Samples were imaged using a confocal microscope for cell nuclei (DAPI, excitation laser 405nm), chitosan (FITC, excitation laser 488nm), and collagen (polarized light). The interpenetration depth was defined as the distance by which the FITC channel overlapped the collagen channel.

Friction Assessment.

Cyclic friction experiments were completed using two actuators with load cells positioned perpendicular to one another. The top actuator applied an 8N normal force, similar to the normal forces experienced in human wrists with a 1kg force applied to the thumb[80]. During normal force application, the horizontal actuator moved in a cyclic triangle waveform (±10mm, 2mm/s) for 500 cycles. 100μl of 1xPBS was applied to the interface every 10 minutes to maintain sample hydration. Load and displacement data for both actuators were acquired and a custom MATLAB script computed the kinetic coefficient of friction during cyclic loading from the normal and friction forces. The coefficient of kinetic friction was compared between contact of the JTA-JTA, JTA-tendon, and tendon-tendon surfaces.

Patellar Tendon Defect Model.

The effect of JTA implantation on uninjured and injured tendons was evaluated in F344XBN rats (age: 8 months; body weight: 400–500g; National Institute on Aging) (N=8/group) (Harvard University IACUC approved). JTA gel disks (diameter 4mm, thickness 0.5mm) were prepared using aseptic techniques and adhered to the central midsubstance of patellar tendons (IACUC approved). To evaluate the effect of the JTA on tendon healing, rats received bilateral full-thickness-partial-width (~50%) excisional injuries to their patellar tendons prior to JTA placement and were euthanized 3-weeks post injury and JTA

placement. Briefly, animals were anesthetized with isoflurane (2–2.5 vol%) while an 8 mm incision through skin superficial to the patellar tendon was made. For tendon injury, the retinaculum on either side of the patellar tendon was cut and a spatula coated with a rubber backing was placed deep to the tendon. A 2 mm biopsy punch was then used to create a full thickness partial width defect in the central patellar tendon midsubstance. In both uninjured and injured animals, the JTA was then implanted in the tendon midsubstance. Gentle pressure on the JTAs was applied for 4 minutes during which adhesion was generated. The skin was then closed with a 4–0 Vicryl suture and animals were returned to cage activity during which post-operative buprenorphine (0.05mg/kg, Buprenex) was given subcutaneously every 12 hours for three days. For drug delivery experiments, similar procedures were performed on female Sprague Dawley rats (age: 16 weeks; body weight: 300–350g, Charles River Laboratories) (N=24). Following surgery, a single dose of sustained release buprenorphine (72h release) (0.5mg/kg, ZooPharms) was given.

To characterize release of the triamcinolone acetonide and its effect, as well as on the inflammatory responses to the adhesive, we evaluated the JTA with and without triamcinolone acetonide loading in a patellar tendon defect model in rats over a 2-week implantation (n=6 rats/group). For analytics of triamcinolone acetonide release, blood glucose levels, endogenous corticosterone, and chemokines, serial serum samples were generated from peripheral blood (50–100ml), obtained from rats during tail vein bleeding. Blood samples were collected in the absence of anticoagulants and allowed to coagulate for 20 to 30 min at room temperature. Samples were then separated by centrifugation, aliquoted, and stored at −80°C prior to analysis. After euthanasia, tendons were harvested, fixed in 4% PFA and decalcified for 1-week prior to paraffin embedding and sectioning (5μm). Histology sections were stained with H&E and immunohistochemistry performed for markers of immune cells (CD45), macrophages (CD68), vascularity (CD31), fibrosis (aSMA), tendon stem/progenitor cells (CD146), M1 macrophages (iNos), and M2 macrophages (Arg-1). Collagen density was examined with multiphoton second harmonic generation (SHG) imaging.

Images were evaluated in CellProfiler[81] for the percent positive cells for each marker. Endogenous corticosterone levels were determined using LS-MS/MS. Serum chemokines were assessed using a Luminex assay. The effect of treatment on percent positive cells, SHG signal, chemokines, and endogenous corticosterone levels was evaluated using one-way ANOVAs with post hoc Tukey tests for multiple comparisons.

The chemokines RANTES and GROα were measured after 2 and 14 days using the commercially available Chemokine Rat ProcartaPlex™ Panel (Invitrogen, Vienna, Austria). Measurements were performed on a Luminex platform, using a Luminex 200 technology instrument (Luminex Copr., Austin, TX, USA) according to the manufacturer's instructions. Calibrations and validations were performed prior to measurements. Mean fluorescence intensities were calculated from duplicate samples.

For longitudinal assessment of JTA adhesion, female Sprague Dawley rats at 16 weeks of age (IACUC approved) were used. A skin incision around the knee was made and a 4mm diameter JTA was implanted on the patellar tendon midsubstance. The skin was closed, and

animals were followed longitudinally using high frequency ultrasound (HFUS) to examine JTA placement.

Supraspinatus Tenotomy.

Adult female Sprague Dawley rats (age: > 6 months; body weight: 300 to 400g) were used. Aseptic surgical procedures were performed under general inhalation anesthesia with isoflurane (1.5–3 vol%). A 15-mm skin incision was made from the acromion towards the humerus bone using a scalpel to expose the deltoid muscle. A 10-mm split of the deltoid muscle was then performed from the humerus towards the acromion to expose the acromion and humeral head. The supraspinatus tendon was pulled from the subacromial space with spinal cord hooks and kept under moderate tension. To create the full thickness partial tenotomy, a 23G cannula was positioned along the long axis of the tendon to guide cutting using a scalpel. To implant the JTA (length 6mm, width 2mm), the shoulder was abducted, and the acromion elevated to allow positioning of the JTA. The JTA was positioned over the supraspinatus enthesis and tendon, and deep to the acromion for additional anchoring. Pressure was applied for 4-minutes using a thin spatula after which the acromion was lowered. The deltoid muscle was then closed by a continuous suture and the skin by a continuous intra-cutaneous suture (Safil 6–0). After recovery from anesthesia, rats returned to cage activity and received buprenorphine (0.05mg/kg, Temgesic) subcutaneously every 6 to 12 hours for three days for post-operative analgesia. Experiments were conducted according to the Swiss laws for animal experimentation and following approval by the veterinarian authorities from the Canton of Basel-Stadt.

High Frequency Ultrasound Imaging (HFUS).

HFUS (Vevo 770 Scanner; 35MHz (RMV712); axial resolution: 50μm, lateral resolution: 140μm, depth of view: 15mm; VisualSonics, Toronto, Canada) was used to evaluate gel swelling in vivo, tendon cross sectional area, and tendon echogenicity in the axial plane. Briefly, after sacrifice, rats were positioned supine on a stage. Knees were shaved and hair was removed using depilatory cream. For imaging of hydrogels, ultrasound images were acquired every 0.5mm throughout the hydrogel diameter (~4mm). For analysis, hydrogels were segmented in MATLAB (vR2017a; Mathworks, Natick MA) and the three centermost images were averaged for JTA thickness. For tendon images, tissues were first fine dissected prior to mounting in a 3D printed device to maintain horizontal orientation of the unloaded patellar tendon. Samples were submerged in a 1x PBS bath during imaging. Axial images were acquired every 0.5mm throughout the length of the tendon. For analysis of tendon morphology, tendon sections were segmented from each image slice in MATLAB (vR2017a; Mathworks, Natick, MA) and the three centermost images were evaluated for the cross-sectional area and echogenicity[82].

High Frequency Doppler Ultrasound Imaging.

High frequency Doppler ultrasound imaging (Vevo 3100 Scanner; 50MHz transducer; axial resolution: 20μm, depth of view: 15mm; VisualSonics, Toronto, Canada) was used to evaluate placement of JTA and vascularity longitudinally in live animals. Briefly, animals were anesthetized with 1.5–2.5% isoflurane and kept supine on a heated platform during imaging. Knees were shaved and hair was removed using depilatory cream. Vital signs

were taken to respiratory gate image acquisition during breathing. The knee was bent at approximately 90^{o} while B-mode and Doppler images in the axial plane were taken using a motorized transducer (0.25mm increments) throughout the length of the patellar tendon (~8mm). Data were analyzed in VevoLab (VisualSonics) using the Doppler ultrasound module to compute total vessel volume in segmented images.

Magnetic Resonance Imaging (MRI).

In vivo serial MRI measurements were performed with a Pharmascan 7 Tesla scanner (Bruker Medical Systems, Ettlingen, Germany). Following an induction period with isoflurane 4%, during acquisitions rats were anesthetized with isoflurane 1.5–2%. Sagittal and axial images were acquired using a Turbo-RARE sequence (effective echo time 21ms, repetition time 5600ms, RARE factor 4, field-of-view 4×3cm (sagittal) or 3×4cm (axial), matrix 256×192, slice thickness 0.4mm, 30 slices) to evaluate the anatomical position of the JTA over time and to assess inflammatory tissue response to the JTA. Maintenance of position of the JTA over time was evaluated by comparing the position of the JTA relative to its location immediately following surgery. Changes in the normalized T2-weighted signal within the supraspinatus tendon was compared over time to determine potential inflammation (higher T2-weighted signal indicates fluid as an indicator for inflammation).

Multiphoton Second Harmonic Generation (SHG) Imaging.

For multiphoton imaging of collagen in healing tendon, a Two-Photon Microscope (Zeiss, LSM 980 NLO) was used (Laser: Spectra-Physics X3 InSight IR tuned to 920 nm; Objective: 25× 0.8 NA multi-immersion LD-LCI lens; Condenser: 1.2 NA water immersion). Forward scatter was collected on a Transmitted Light-PMT multi-alkali detector. Reverse scatter was detected with a Non-descanned GaAsP detector behind a CFP (440–480 nm) emission filter. Mean intensities for SHG signal was processed between groups in MATLAB.

In Vitro Cell Viability.

Tendon cells were isolated from the Male F344XBN rats at 8 months of age acquired from the National Institute of Aging[83]. Rats were euthanized and flexor digitorum longus tendons with the surrounding paratenon and epitenon were dissected using sterile technique and kept on ice in Dulbecco's Modified Eagle's Medium (DMEM) (Invitrogen). Tendons were then minced and digested in 0.5% type I collagenase (Worthington) and 4U/ml dispase (Stem Cell Technologies) in HBSS for 4 hours at 37°C. From digests, cells were strained, collected, and resuspended in media[84]. Tendon cells were cultured in DMEM with 10% Fetal Bovine Serum (Invitrogen) and 1% penicillin/streptomycin (Invitrogen). For cytocompatibility testing in the presence of the tough gel, tendon derived cells were incubated with or without tough hydrogels (diameter 3mm, thickness 1.5mm) for 1 and 2 days. For cytocompatibility testing in the presence of triamcinolone acetonide releasing gels, tendon derived cells were incubated with tough hydrogels containing 0μg, 0.53μg, or 0.212μg of CORT (diameter 3mm or 6mm, thickness 1.5mm at 10mg/ml loading) (Supplementary Fig. 7). Cell viability was assessed by trypan blue staining[85] after incubating gels containing triamcinolone acetonide in transwells and quantified using an

automated counter (Countess II Automated Cell Counter system, ThermoFisher, Waltham, MA).

Dynamic Mechanical Testing.

Three weeks post injury and/or JTA implantation, patella-patellar tendon-tibia samples were harvested and fine dissected. Briefly, surrounding musculature, adipose tissue, and non-tendon connective tissue were carefully removed using stereomicroscopy while maintaining tissue hydration (1x PBS). Fine dissected tendon samples were then stamped into a dog bone shape to isolate the injury region, leaving a 2mm width at the center. Tendons were then imaged using HFUS to determine their echogenicity and cross-sectional area while being submerged in 1x PBS. For mechanical testing, tendons were secured in custom fixtures submerged in a 1xPBS bath. Briefly, the tibial end was mounted in an acrylic pot using liquid metal and the patellar end was gripped in a custom fixture to secure the patella in a manner which did not stress the tendon. The samples were mounted while submerged in a 1x PBS bath at room temperature in a dynamic mechanical testing frame (Electroforce 3200, TA Instruments, Minnesota). A comprehensive mechanical test was then completed to evaluate tendon viscoelastic, dynamic, and quasi-static mechanical properties (Supplementary Fig. 3a). Briefly, samples underwent preloading (0.1N), preconditioning (30 cycles at 0.25–0.5% strain), stress relaxation (4% strain), a dynamic frequency sweep (0.1, 1, 5, and 10Hz) at a strain amplitude of 0.125%, and a ramp to failure (0.05%strain/s) using a 225N load cell. Displacement and force data collected during loading were processed using custom MATLAB software (vR017a; Mathworks, Natick, MA) to compute the percent relaxation, relaxation half time, dynamic modulus, tanδ, toe modulus, linear modulus, transition strain, and failure stress[52,86–88].

Patellar Tendon Histology.

Patellar tendons were collected and immersed in 4% PFA for 24 hours before being washed in 1xPBS and transferred to 70% ethanol. Samples were then processed, embedded in paraffin, and sectioned (5μm) in the sagittal plane. Tissue sections were then stained with hematoxylin and eosin and imaged (Axiozoom Tissue Scanner, Zeiss, Germany). Images were then processed using CellProfiler for cellularity and nuclear shape. Briefly, after cropping the region of interest, a color deconvolution algorithm was applied to separate the histological stains based on absorbance values. Next, the deconvolved hematoxylin image was processed with a two class Otsu thresholding algorithm to identify and segment the cell nuclei. Lastly, a processing module was applied to extract nuclear area, shape, and number.

Supraspinatus Tendon Histology.

Following the last MRI imaging, rat shoulders were collected and immersed for 72 hours in 10% neutral buffered formalin (NBF), and then transferred to a decalcification solution (ImmunoCal #1440, Decal Chemical Corp, Suffern, NY) for 5–7 days with daily changes, until decalcification was complete as verified chemically using a procedure previously described[89]. After bisection in the coronal anatomic plane to expose the mid-plane of the rotator cuff, samples were dehydrated and paraffin embedded. Next, 5-μm thick coronal sections were obtained and stained with hematoxylin (3 minutes) and eosin (30 seconds) (H&E) using a ST5010 Autostainer XL (Leica) and mounted in Pertex (#41–4011-00,

Medite). HE-stained slides were scanned with an Aperio slide scanner (Leica) for general observations.

JTA Implantation on Rat Achilles Tendon.

Female Sprague Dawley rats (N=9–10/group) at 16-weeks of age were used (IACUC approved). Animals were housed in a conventional facility (12-hour light/dark cycles), fed standard chow, and were provided water ad libitum. Surgical intervention used sterile techniques under anesthesia (Isoflurane) to bluntly transect the right Achilles tendon midsubstance and resect the plantaris longus tendon. Animals were given a single dose of sustained release buprenorphine (0.3 mL, 1mg/ml) prior to surgery. Following injury all animals received repair treatment (Urbaniak variant of the Kessler) (6), with (n=10) or without (n=9) JTA implantation. All injured hind limbs were immobilization in plantar flexion using stirrups, a laser cut acrylic splint, Webril padding, CoFlex, and poly(methyl-methacrylate), with all casts checked daily (6). Uninjured contralateral limbs were used as controls. Animals were euthanized 3-weeks post-injury (CO2 inhalation) and tissues were harvested. Tendons were harvested and prepared for ultrasound imaging and mechanical testing, as described [88]. Briefly, custom fixtures were used to grip the bone-tendon unit to maintain the Achilles tendon-foot complex in a perpendicular orientation during loading. These fixtures were mounted to a testing frame (Electroforce 3200, TA Instruments) while specimens were submerged in a 1x PBS bath. During loading, force and displacement data were acquired using WinTest (TA Instruments) and processed using MATLAB. Achilles tendon percent relaxation, dynamic modulus (|E*|), tanδ, toe- and linear- modulus, and failure were evaluated[52,86–88,90].

Drug Loading and Release.

Micronized triamcinolone acetonide (CORT) morphology was assessed using scanning electron microscopy. Tough hydrogels (thickness 0.75mm, diameter 3mm) were loaded with 1, 10, or 100mg/ml CORT (Toronto Research Chemical or Sandoz) and examined for release in sink conditions (HBSS, pH 7.4). Sink conditions were defined as the required volume of water to solubilize the entire loaded amount of CORT within the tough hydrogel. This release buffer was maintained at 37°C on a shaker and was subsequently sampled and replaced daily to maximize the flux of drug out of the tough hydrogel. Released drug was sampled daily and evaluated using liquid chromatography-mass spectrometry (Agilent 1290/6140, Gradient method; SIM mode). Chromatographic separation was performed at room temperature using an HPLC column (Agilant Zorbax Rx-C18; internal diameter 2.1mm, length 150mm). A two-solvent linear gradient method was used (A:0.02% formic acid; B:methanol). Drug concentration was quantified by integrating the characteristic peak.

The stretchability and adhesion of the CORT incorporated hydrogel was measured in the native form. Prior to implantation, the hydrogel was pre-swollen and strong adhesion was observed (Supplementary Fig. 2).

Quantitative Determination of Endogenous Corticosterone.

Sample preparation and analysis was based on a modified protein precipitation procedure followed by liquid chromatographic separation coupled with mass spectrometry for

detection. 10μl serum samples were diluted with 20μl EDTA (0.75 mg/ml K2EDTA in 0.9% NaCl solution). Calibration, quality control, and recovery control samples were prepared by spiking blank charcoal stripped bovine serum (Sigma-Aldrich, #F6765) with known quantities of corticosterone (between 5 and 12'500ng/mL). For corticosterone determination, dexamethasone was used as generic internal standard (IS). Aliquots of 30μL calibration standard, quality control, recovery control, and unknown samples were transferred to 0.75ml 96- well- Loborack (Vitaris AG, # 51004BC -MIC) and 2μL IS mixture (2.5μg/mL in CH_3OH) was added to each tube. For protein precipitation and extraction from serum, 100μl CH_3CN was added. After vortexing for 3 minutes, the samples were centrifuged at 3220g for 15min at 4°C. 100μl of the upper layer was transferred to a 1.2mL 96 deep well plate (Thermo Scientific, # AB-0787) and evaporated to dryness using N2 gas stream at 60°C. Then the residues were resuspended with 100μL CH_3OH/H_2O (1/1; v/v) acidified with 0.1% formic acid.

LC-MS/MS analysis: For quantitative analysis, a 10μl aliquot of each sample, including calibration, quality control, and recovery control samples were injected with a cooled Shimadzu Nexera X2 LC-30 AD HPLC system. The corticosterone and dexamethasone were separated with a Phemomenex Synergi polar RP (50 × 2.1mm ID, 2.5μm particle size) as column at 60°C. For separation a linear gradient from 10% to 65 % B in 3.0 min at a flow rate of 0.400 mL/min was applied. The total cycle time was 5.5min. The mobile phase used was A: water with 0.1 % formic acid, and B: CH3OH with 0.1 % formic acid. For detection, the column effluent was directly guided in an AB Sciex API6500 Triple quad mass spectrometer equipped with a TurboIonSpray interface. The detection was done in MRM positive ion mode. Quantification was based on the compound/IS ratio of the extracted ion chromatograms of the selected mass transitions 347 m/z → 329, 121, 91 m/z for LLX393 and 393 m/z → 355, 372 m/z for XAC401 (IS). The unknown sample concentration was calculated using external calibration curves. The LLOQ of the method was set to 5 ng/mL for serum. The recovery from the matrix was 102±3 % for corticosterone and 89±10 % for dexamethasone (IS). All calculations were performed with AB Sciex Analyst software.

Computational Modeling

Franz Cell Simulations—Diffusion of dissolved triamcinolone acetonide in the unloaded tough hydrogel was modelled and matched with wet-bench diffusion data derived from standard unjacketed Franz diffusion cell experiments performed at room temperature. The volume of the donor compartment was 1ml (unstirred) and the volume of the acceptor compartments was 5ml (well-stirred). The starting concentration of triamcinolone acetonide in the donor compartment was 20μg/ml (Fig. C). The donor compartment was separated from the acceptor compartment either by a PVDF membrane [mechanical support for the hydrogel, thickness 125μm, pore size 0.45μm, porosity 70%, (Durapore NF-HVLP02500)] or a combination of the PVDF membrane and the hydrogel (thickness 750μm).

The time transient diffusion equation (Eq 2) was solved in 2D axissymmetric form, using the concentration c and the diffusion constant D. The acceptor compartment was well stirred, thus the diffusion constant was set large enough to enforce instant distribution[91]. In contrast,

the donor compartment was unstirred and the diffusion constant of triamcinolone acetonide in water was approximated to 436μm^2/s at 20°C [92].

Wet-bench diffusion data were used to adjust the simulated apparent diffusion constants of dissolved triamcinolone acetonide in the unloaded tough hydrogel. The simulated apparent diffusion constant of triamcinolone acetonide in the PVDF membrane was 305μm^2/s. In a second simulation, the apparent diffusion constant in the PVDF membrane was fixed and the apparent diffusion constant of triamcinolone acetonide in the hydrogel was 16μm^2/s.

Dissolution and Transport Kinetics of Triamcinolone from the JTA—To simulate the dissolution and transport kinetics of embedded triamcinolone acetonide crystals from the dissipative hydrogel under sink conditions, a 3D Finite Element Model (FE-model) was developed using the module “Transport of Diluted Species” of the Finite Element Software COMSOL Multiphysics (Release 5.5). In the 3D FE-model, each spherical triamcinolone acetonide crystal was surrounded by a cubical volume of the hydrogel. The FE-model consisted of 8 cubical units with a side length of 46.8μm resulting in a total length of 375μm of the FE-model probe. The FE-model probe had symmetry conditions on all sides, except at the interface to the acceptor compartment. The acceptor compartment was modelled as a well-stirred water-filled compartment with the total volume replaced every 24 hours. At time point ‘zero’ of the simulation, the concentration of triamcinolone acetonide was set to zero in the hydrogel and the acceptor compartment. With this modular approach, the dissolution and transport kinetics of triamcinolone acetonide crystal, embedded in the hydrogel was simulated at the two triamcinolone acetonide loadings of 10mg/ml and 100mg/ml.

Dissolution of embedded triamcinolone acetonide crystals at the crystal hydrogel phase boundary was modelled in thermodynamically equilibrium using the maximum solubility of triamcinolone acetonide. The mass flux of triamcinolone was calculated by Fick’s law, with the main variable’s diffusion constant and solubility in the hydrogel phase (Eq 1).

$$Csol_{(water,\,37°C)} = 33\ \mu g/ml \qquad \text{(Eq 1)}$$

With progressing dissolution, the embedded triamcinolone acetonide spherical crystals were modeled to shrink in diameter. This change in geometry of the spherical crystals and the consequence on dissolution of triamcinolone acetonide crystals at the crystal hydrogel phase boundary was modelled by a moving interface. The outer shape of the hydrogel was fixed.

Dissolution and diffusion of triamcinolone acetonide (10mg/ml and 100mg/ml) embedded as spherical crystals in the hydrogel to a well-stirred water-filled acceptor compartment was modelled and matched with wet-bench transport kinetic data at 37°C. The time transient 3D diffusion equation (2) was solved, using the concentration c and the diffusion constant D (Eq 2).

$$\frac{\partial c}{\partial t} - \nabla \cdot (D \nabla c) = 0 \qquad \text{(Eq 2)}$$

Because well-stirring was applied in the acceptor compartment, the diffusion constant in the acceptor compartment was set large enough to enforce instant distribution [91]. Wet-bench transport kinetic data were used to adjust the simulated apparent diffusion constants of triamcinolone acetonide in the drug-loaded hydrogel. Following dissolution of triamcinolone acetonide crystals embedded in the hydrogel (Csol = 33μg/ml), the simulated apparent diffusion constants increased with drug load, from 153$\mu m^2/s$ (10mg/ml) to 273$\mu m^2/s$ (100mg/ml). In comparison, the diffusion constant of triamcinolone acetonide in water is reported to be 673$\mu m^2/s$[42]. We speculate that as drug loading increases to be similar or greater than the tough gel's polymer content, larger cavities are generated as drug particles dissolve. This, in turn, increases the overall diffusivity due to the aqueous solution filling the cavities created by drug dissolution.

Flexor Tendon Testing in Human Cadavers.

Human fore limbs were surgically prepared using an LCP Volar Rim Distal Radius (LLP) (DePuy Synthes, West Chester, PA). The distal radius was approached using a volar incision over the flexor carpi radialis tendon. After elevation of the pronator quadratus muscle, the implant was fixed to the distal radius using a single cortical screw in an oblong hole. Plates were positioned at Soong 0 (pVA-LCP) or Soong 2 (dVA-LCP) position relative to the watershed line and the position was confirmed with fluoroscopy. No fractures were created in this model. Distal row locking holes were filled using a fixed angle guide with 2.4mm diameter screws that were sized appropriately for the specimen. The pronator quadratus was excised to mimic irreparable disruption observed after distal radius fractures. JTAs ($10\times40\times1mm^3$) were adhered to the underside of the flexor digitorum profundus tendon. Flexion/extension of the thumb was used to test their attachment and ability to glide over the volar plate and transverse carpal ligaments.

Statistical Analysis.

Data normality was assessed with Shapiro Wilk tests (SPSS). One-way (time) or two-way (healing and JTA implantation) ANOVA tests were used to evaluate the effects of time, injury, or treatment on all properties assessed. Significant factors were evaluated using post hoc Student's t-tests with Bonferroni corrections for multiple comparisons.

Reporting Summary.

Further information on research design is available in the Nature Research Reporting Summary linked to this article. Supplemental figures, supplemental movies, a supplemental table, and extended data is available.

Data availability

The main data supporting the results in this study are available within the paper and its Supplementary Information. Source data for the figures are provided with this paper. All raw and analysed datasets generated during the study are available for research purposes from the corresponding authors on reasonable request.

Code availability

MATLAB code used to process mechanical data is available on reasonable request, and we will ensure its compatibility with any study-specific datasets generated.

Extended Data

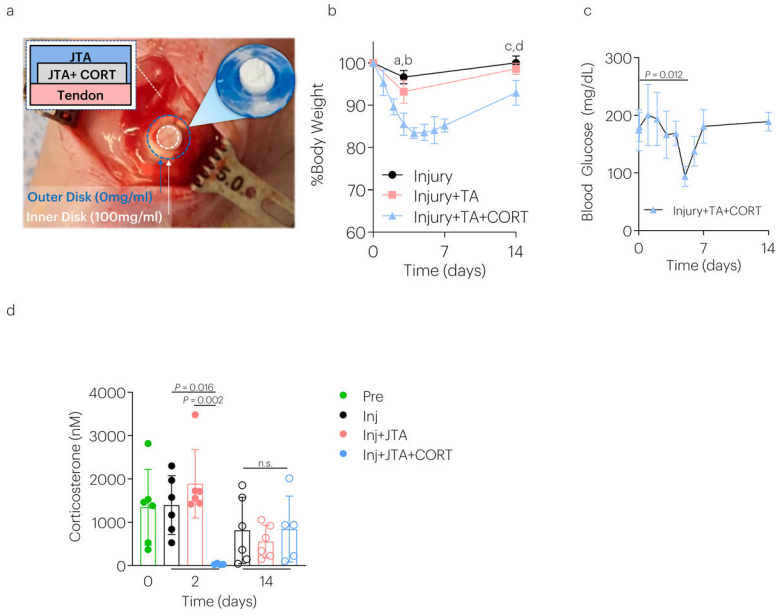

ED Fig. 1. Effect of CORT releasing JTAs on animal physiology over time.

(a) The JTA dissolution-controlled release system was surrounded by an outer JTA to stabilize it on the rat patellar tendon and enable a depot-based delivery system. (b) Rat body weight was examined over time. Data shown as mean ± s.d., as analyzed by ANOVAs, with post hoc tests with Bonferroni corrections. a: P = 0.0008, b: P = 0.002; c: P = 0.006; d: P = 0.0011. N=4–6 rats/group. (c) Blood glucose levels were evaluated over time. Data shown as mean ± s.d., as evaluated by a one-way ANOVA, with post hoc Tukey Tests for multiple comparisons. N=4–6 rats/group. (d) The effect of injury, JTA, and CORT on corticosterone levels 2 days and 14 days post-implantation. Data shown as mean ± s.d., as analyzed by a two-way repeated ANOVA (time and treatment), with post hoc Tukey Tests for multiple comparisons. N=4–6 samples/group.

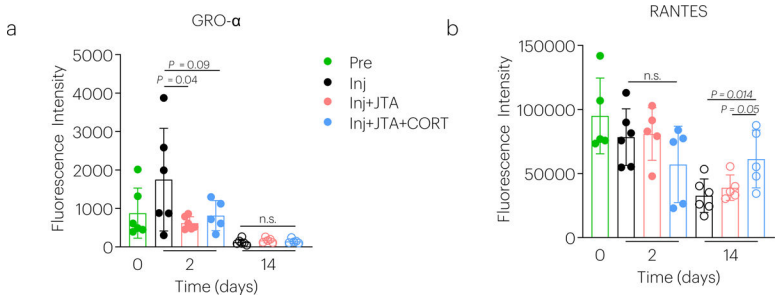

ED Fig. 2. Effect of the JTA and corticosteroid delivery on chemokines.

The effect of injury, JTA, and CORT on (a) GROα and (b) RANTES was evaluated after 2 and 14 days of healing. Data shown as mean ± s.d., as evaluated by a two-way repeated measures ANOVA with post hoc Tukey Tests for multiple comparisons. N=5–6 samples/group.

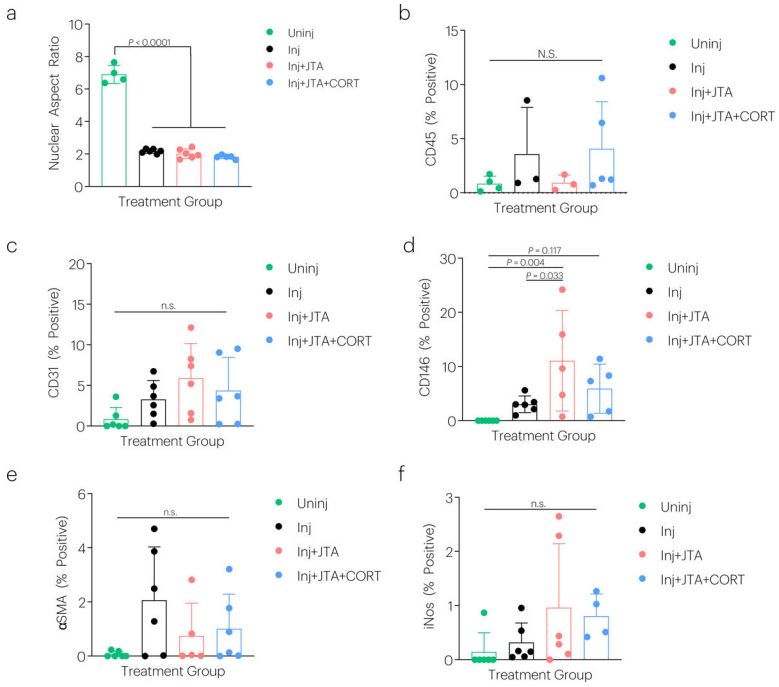

ED Fig. 3. Effect of the JTA and corticosteroid delivery on tendon histological properties.
The effect of injury, JTA, and CORT on (a) nuclear aspect ratio, (b) CD45, (c) CD31, (d) CD146, (e) αSMA, and (f) iNos staining was evaluated after 2-weeks of healing. Data shown as mean ± s.d., as evaluated by a one-way ANOVA with post hoc Tukey Tests for multiple comparisons. N=4–6 tendons/group.

Supplementary Material

Refer to Web version on PubMed Central for supplementary material.

Acknowledgements

This work was supported by the National Institute on Aging of the NIH (F32AG057135, K99AG065495), Novartis, and the Wyss Institute for Biologically Inspired Engineering. Porcine tissues *ex vivo* was donated by Boston Children's Hospital. We thank Michael Lewandowski and the Harvard Center for Biological Imaging for discussion.

Competing interests

The authors receive grant support through Novartis. The views and opinions expressed in this article are those of the authors and do not necessarily reflect the position of the Wyss Institute for Biologically Inspired Engineering at Harvard University nor Novartis.

References

1. Surgeons A. A. o. O. Optimizing the Management of Rotator Cuff Problems. (2013).

2. Iannotti JP Full-Thickness Rotator Cuff Tears: Factors Affecting Surgical Outcome. J Am Acad Orthop Surg 2, 87–95 (1994). [PubMed: 10708996]

3. Goutallier D, Postel JM, Gleyze P, Leguilloux P & Van Driessche S Influence of cuff muscle fatty degeneration on anatomic and functional outcomes after simple suture of full-thickness tears. J Shoulder Elbow Surg 12, 550–554, doi:10.1016/S1058274603002118 (2003). [PubMed: 14671517]

4. McCarron JA et al. Failure with continuity in rotator cuff repair “healing”. Am J Sports Med 41, 134–141, doi:10.1177/0363546512459477 (2013). [PubMed: 23019253]

5. Rodeo SA Biologic augmentation of rotator cuff tendon repair. J Shoulder Elbow Surg 16, S191–197, doi:10.1016/j.jse.2007.03.012 (2007). [PubMed: 17574875]

6. Watts AE et al. MicroRNA29a Treatment Improves Early Tendon Injury. Mol Ther 25, 2415–2426, doi:10.1016/j.ymthe.2017.07.015 (2017). [PubMed: 28822690]

7. Millar NL et al. MicroRNA29a regulates IL-33-mediated tissue remodelling in tendon disease. Nat Commun 6, 6774, doi:10.1038/ncomms7774 (2015). [PubMed: 25857925]

8. Li J et al. Tough Composite Hydrogels with High Loading and Local Release of Biological Drugs. Adv Healthc Mater 7, e1701393, doi:10.1002/adhm.201701393 (2018). [PubMed: 29441702]

9. Gelberman RH et al. Combined Administration of ASCs and BMP-12 Promotes an M2 Macrophage Phenotype and Enhances Tendon Healing. Clin Orthop Relat Res 475, 2318–2331, doi:10.1007/s11999-017-5369-7 (2017). [PubMed: 28462460]

10. Freedman BR & Mooney DJ Biomaterials to Mimic and Heal Connective Tissues. Adv Mater 31, e1806695, doi:10.1002/adma.201806695 (2019). [PubMed: 30908806]

11. Murray MM et al. The Bridge-Enhanced Anterior Cruciate Ligament Repair (BEAR) Procedure: An Early Feasibility Cohort Study. Orthop J Sports Med 4, 2325967116672176, doi:10.1177/2325967116672176 (2016). [PubMed: 27900338]

12. Shoaib A & Mishra V Surgical repair of symptomatic chronic achilles tendon rupture using synthetic graft augmentation. Foot Ankle Surg 23, 179–182, doi:10.1016/j.fas.2016.04.006 (2017). [PubMed: 28865587]

13. Mitragotri S, Burke PA & Langer R Overcoming the challenges in administering biopharmaceuticals: formulation and delivery strategies. Nat Rev Drug Discov 13, 655–672, doi:10.1038/nrd4363 (2014). [PubMed: 25103255]

14. Anselmo AC & Mitragotri S Nanoparticles in the clinic: An update. Bioeng Transl Med 4, e10143, doi:10.1002/btm2.10143 (2019). [PubMed: 31572799]

15. Li J & Mooney DJ Designing hydrogels for controlled drug delivery. Nat Rev Mater 1, doi:10.1038/natrevmats.2016.71 (2016).

16. Bjarnason I, Hayllar J, MacPherson AJ & Russell AS Side effects of nonsteroidal anti-inflammatory drugs on the small and large intestine in humans. Gastroenterology 104, 1832–1847, doi:10.1016/0016-5085(93)90667-2 (1993). [PubMed: 8500743]

17. Svanstrom H, Lund M, Melbye M & Pasternak B Concomitant use of low-dose methotrexate and NSAIDs and the risk of serious adverse events among patients with rheumatoid arthritis. Pharmacoepidemiol Drug Saf, doi:10.1002/pds.4555 (2018).

18. Blomquist J, Solheim E, Liavaag S, Baste V & Havelin LI Do nonsteroidal anti-inflammatory drugs affect the outcome of arthroscopic Bankart repair? Scand J Med Sci Sports 24, e510–514, doi:10.1111/sms.12233 (2014). [PubMed: 24750379]

19. Soreide E et al. The Effect of Limited Perioperative Nonsteroidal Anti-inflammatory Drugs on Patients Undergoing Anterior Cruciate Ligament Reconstruction. Am J Sports Med 44, 3111–3118, doi:10.1177/0363546516657539 (2016). [PubMed: 27496908]

20. Oh JH et al. Do Selective COX-2 Inhibitors Affect Pain Control and Healing After Arthroscopic Rotator Cuff Repair? A Preliminary Study. Am J Sports Med 46, 679–686, doi:10.1177/0363546517744219 (2018). [PubMed: 29253346]

21. Kwon HH et al. Synergistic effect of cumulative corticosteroid dose and immunosuppressants on avascular necrosis in patients with systemic lupus erythematosus. Lupus, 961203318784648, doi:10.1177/0961203318784648 (2018).

22. Wang JC, Chang KV, Wu WT, Han DS & Ozcakar L Ultrasound-Guided Standard vs Dual-Target Subacromial Corticosteroid Injections for Shoulder Impingement Syndrome: A Randomized

Controlled Trial. Arch Phys Med Rehabil 100, 2119–2128, doi:10.1016/j.apmr.2019.04.016 (2019). [PubMed: 31150601]

23. Hugate R, Pennypacker J, Saunders M & Juliano P The effects of intratendinous and retrocalcaneal intrabursal injections of corticosteroid on the biomechanical properties of rabbit Achilles tendons. J Bone Joint Surg Am 86, 794–801, doi:10.2106/00004623-200404000-00019 (2004). [PubMed: 15069146]
24. Zhang B, Hu ST & Zhang YZ Spontaneous rupture of multiple extensor tendons following repeated steroid injections: a case report. Orthop Surg 4, 118–121, doi:10.1111/j.1757-7861.2012.00170.x (2012). [PubMed: 22615159]
25. Markl D & Zeitler JA A Review of Disintegration Mechanisms and Measurement Techniques. Pharm Res 34, 890–917, doi:10.1007/s11095-017-2129-z (2017). [PubMed: 28251425]
26. Li J et al. Tough adhesives for diverse wet surfaces. Science 357, 378–381, doi:10.1126/science.aah6362 (2017). [PubMed: 28751604]
27. Linderman SW et al. Shear lag sutures: Improved suture repair through the use of adhesives. Acta Biomater 23, 229–239, doi:10.1016/j.actbio.2015.05.002 (2015). [PubMed: 26022966]
28. Evans CE, Lees GC & Trail IA Cytotoxicity of cyanoacrylate adhesives to cultured tendon cells. J Hand Surg Br 24, 658–661, doi:10.1054/jhsb.1999.0279 (1999). [PubMed: 10672798]
29. Zhao C et al. CORR(R) ORS Richard A. Brand Award for Outstanding Orthopaedic Research: Engineering flexor tendon repair with lubricant, cells, and cytokines in a canine model. Clin Orthop Relat Res 472, 2569–2578, doi:10.1007/s11999-014-3690-y (2014). [PubMed: 24906811]
30. Zhao C et al. Surface modification counteracts adverse effects associated with immobilization after flexor tendon repair. J Orthop Res 30, 1940–1944, doi:10.1002/jor.22177 (2012). [PubMed: 22714687]
31. Mellstrand-Navarro C, Pettersson HJ, Tornqvist H & Ponzer S The operative treatment of fractures of the distal radius is increasing: results from a nationwide Swedish study. The bone & joint journal 96-b, 963–969, doi:10.1302/0301-620x.96b7.33149 (2014). [PubMed: 24986952]
32. Soong M, Earp BE, Bishop G, Leung A & Blazar P Volar locking plate implant prominence and flexor tendon rupture. The Journal of bone and joint surgery. American volume 93, 328–335, doi:10.2106/jbjs.J.00193 (2011).
33. Tang JB Clinical outcomes associated with flexor tendon repair. Hand Clin 21, 199–210, doi:10.1016/j.hcl.2004.11.005 (2005). [PubMed: 15882599]
34. Strickland JW Development of flexor tendon surgery: twenty-five years of progress. J Hand Surg Am 25, 214–235, doi:10.1053/jhsu.2000.jhsu25a0214 (2000). [PubMed: 10722813]
35. May EJ & Silfverskiold KL Rate of recovery after flexor tendon repair in zone II. A prospective longitudinal study of 145 digits. Scand J Plast Reconstr Surg Hand Surg 27, 89–94, doi:10.3109/02844319309079789 (1993). [PubMed: 8351502]
36. Zhao X Multi-scale multi-mechanism design of tough hydrogels: building dissipation into stretchy networks. Soft Matter 10, 672–687, doi:10.1039/c3sm52272e (2014). [PubMed: 24834901]
37. Sun JY et al. Highly stretchable and tough hydrogels. Nature 489, 133–136, doi:10.1038/nature11409 (2012). [PubMed: 22955625]
38. Riggin CN, Sarver JJ, Freedman BR, Thomas SJ & Soslowsky LJ Analysis of Collagen Organization in Mouse Achilles Tendon Using High-Frequency Ultrasound Imaging. J Biomech Eng, doi:10.1115/1.40262851793821 [pii] (2013).
39. Colvin AC, Egorova N, Harrison AK, Moskowitz A & Flatow EL National trends in rotator cuff repair. J Bone Joint Surg Am 94, 227–233, doi:10.2106/JBJS.J.00739 (2012). [PubMed: 22298054]
40. Soslowsky LJ, Carpenter JE, DeBano CM, Banerji I & Moalli MR Development and use of an animal model for investigations on rotator cuff disease. J Shoulder Elbow Surg 5, 383–392, doi:S1058–2746(96)80070-X [pii] (1996). [PubMed: 8933461]
41. Kosiyatrakul A, Loketkrawee W & Luenam S Different Dosages of Triamcinolone Acetonide Injection for the Treatment of Trigger Finger and Thumb: A Randomized Controlled Trial. J Hand Surg Asian Pac Vol 23, 163–169, doi:10.1142/S2424835518500157 (2018).
42. Seki T et al. Measurement of diffusion coefficients of parabens and steroids in water and 1-octanol. Chem Pharm Bull (Tokyo) 51, 734–736, doi:10.1248/cpb.51.734 (2003). [PubMed: 12808257]

43. Wang JR et al. Polymorphism of Triamcinolone Acetonide Acetate and Its Implication for the Morphology Stability of the Finished Drug Product. Crystal Growth and Design 17, 9, doi:10.1021/acs.cgd.7b00453 (2017).
44. Yang J, Bai R, Chen B & Zuo S Hydrogel Adhesion: A Supramolecular Synergy of Chemistry, Topology, and Mechanics. Advanced Functional Materials, 27 (2019).
45. He M et al. The effect of fibrin glue on tendon healing and adhesion formation in a rabbit model of flexor tendon injury and repair. J Plast Surg Hand Surg 47, 509–512, doi:10.3109/2000656X.2013.789037 (2013). [PubMed: 23621097]
46. Freedman BR, Gordon JA & Soslowsky LJ The Achilles tendon: fundamental properties and mechanisms governing healing. Muscles Ligaments Tendons J 4, 245–255 (2014). [PubMed: 25332943]
47. Zhang K et al. Tendon mineralization is progressive and associated with deterioration of tendon biomechanical properties, and requires BMP-Smad signaling in the mouse Achilles tendon injury model. Matrix Biol 52–54, 315–324, doi:10.1016/j.matbio.2016.01.015S0945-053X(16)30009-9 [pii] (2016).
48. Mienaltowski MJ et al. Injury response of geriatric mouse patellar tendons. J Orthop Res 34, 1256–1263, doi:10.1002/jor.23144 (2016). [PubMed: 26704368]
49. Olsson N et al. Major functional deficits persist 2 years after acute Achilles tendon rupture. Knee Surg Sports Traumatol Arthrosc 19, 1385–1393, doi:10.1007/s00167-011-1511-3 (2011). [PubMed: 21533539]
50. Olsson N et al. Predictors of Clinical Outcome After Acute Achilles Tendon Ruptures. Am J Sports Med 42, 1448–1455, doi:10.1177/0363546514527409036354651452740903 6546514527409 [pii] (2014). [PubMed: 24658347]
51. Freedman BR et al. Mechanical, histological, and functional properties remain inferior in conservatively treated Achilles tendons in rodents: Long term evaluation. J Biomech 56, 55–60, doi:10.1016/j.jbiomech.2017.02.030 (2017). [PubMed: 28366437]
52. Freedman BR, Sarver JJ, Buckley MR, Voleti PB & Soslowsky LJ Biomechanical and structural response of healing Achilles tendon to fatigue loading following acute injury. J Biomech 47, 2028–2034, doi:10.1016/j.jbiomech.2013.10.054 (2014). [PubMed: 24280564]
53. Langer R & Folkman J Polymers for the sustained release of proteins and other macromolecules. Nature 263, 797–800, doi:10.1038/263797a0 (1976). [PubMed: 995197]
54. Sun B, Wang Z, He Q, Fan W & Cai S Porous double network gels with high toughness, high stretchability and fast solvent-absorption. Soft Matter 13, 6852–6857, doi:10.1039/c7sm01102d (2017). [PubMed: 28837202]
55. Fornasiero F, Krull F, Prausnitz JM & Radke CJ Steady-state diffusion of water through soft-contact-lens materials. Biomaterials 26, 5704–5716, doi:10.1016/j.biomaterials.2005.02.028 (2005). [PubMed: 15878376]
56. Kapetanos G The effect of the local corticosteroids on the healing and biomechanical properties of the partially injured tendon. Clin Orthop Relat Res, 170–179 (1982).
57. Yang SL, Zhang YB, Jiang ZT, Li ZZ & Jiang DP Lidocaine potentiates the deleterious effects of triamcinolone acetonide on tenocytes. Med Sci Monit 20, 2478–2483, doi:10.12659/MSM.891116 (2014). [PubMed: 25433272]
58. Blomgran P, Hammerman M & Aspenberg P Systemic corticosteroids improve tendon healing when given after the early inflammatory phase. Sci Rep 7, 12468, doi:10.1038/s41598-017-12657-0 (2017). [PubMed: 28963482]
59. Harada Y et al. Dose- and time-dependent effects of triamcinolone acetonide on human rotator cuff-derived cells. Bone Joint Res 3, 328–334, doi:10.1302/2046-3758.312.2000321 (2014). [PubMed: 25477418]
60. Wong MW, Tang YN, Fu SC, Lee KM & Chan KM Triamcinolone suppresses human tenocyte cellular activity and collagen synthesis. Clin Orthop Relat Res, 277–281, doi:10.1097/01.blo.0000118184.83983.65 (2004).
61. Tempfer H et al. Effects of crystalline glucocorticoid triamcinolone acetonide on cultered human supraspinatus tendon cells. Acta Orthop 80, 357–362, doi:10.3109/17453670902988360 (2009). [PubMed: 19421912]

62. Rudnik-Jansen I et al. Local controlled release of corticosteroids extends surgically induced joint instability by inhibiting tissue healing. Br J Pharmacol 176, 4050–4064, doi:10.1111/bph.14817 (2019). [PubMed: 31378925]
63. Kazimierczak P, Koziol M & Przekora A The Chitosan/Agarose/NanoHA Bone Scaffold-Induced M2 Macrophage Polarization and Its Effect on Osteogenic Differentiation In Vitro. Int J Mol Sci 22, doi:10.3390/ijms22031109 (2021).
64. Ashouri F et al. Macrophage polarization in wound healing: role of aloe vera/chitosan nanohydrogel. Drug Deliv Transl Res 9, 1027–1042, doi:10.1007/s13346-019-00643-0 (2019). [PubMed: 31115868]
65. Papadimitriou L, Kaliva M, Vamvakaki M & Chatzinikolaidou M Immunomodulatory Potential of Chitosan-graft-poly(ε-caprolactone) Copolymers toward the Polarization of Bone-Marrow-Derived Macrophages. ACS Biomater Sci Eng 3, 1341–1349, doi:10.1021/acsbiomaterials.6b00440 (2017). [PubMed: 33429692]
66. Vasconcelos DP et al. Modulation of the inflammatory response to chitosan through M2 macrophage polarization using pro-resolution mediators. Biomaterials 37, 116–123, doi:10.1016/j.biomaterials.2014.10.035 (2015). [PubMed: 25453942]
67. Vasconcelos DP et al. Macrophage polarization following chitosan implantation. Biomaterials 34, 9952–9959, doi:10.1016/j.biomaterials.2013.09.012 (2013). [PubMed: 24074837]
68. Siebelt M et al. Triamcinolone acetonide activates an anti-inflammatory and folate receptor-positive macrophage that prevents osteophytosis in vivo. Arthritis Res Ther 17, 352, doi:10.1186/s13075-015-0865-1 (2015). [PubMed: 26637220]
69. Luvanda MK et al. Dexamethasone Creates a Suppressive Microenvironment and Promotes Aspergillus fumigatus Invasion in a Human 3D Epithelial/Immune Respiratory Model. J Fungi (Basel) 7, doi:10.3390/jof7030221 (2021).
70. Bi Y et al. Identification of tendon stem/progenitor cells and the role of the extracellular matrix in their niche. Nat Med 13, 1219–1227, doi:10.1038/nm1630 (2007). [PubMed: 17828274]
71. Lee CH et al. Harnessing endogenous stem/progenitor cells for tendon regeneration. J Clin Invest 125, 2690–2701, doi:10.1172/JCI81589 (2015). [PubMed: 26053662]
72. Darnell MC et al. Performance and biocompatibility of extremely tough alginate/polyacrylamide hydrogels. Biomaterials 34, 8042–8048, doi:10.1016/j.biomaterials.2013.06.061 (2013). [PubMed: 23896005]
73. Blacklow SO et al. Bioinspired mechanically active adhesive dressings to accelerate wound closure. Sci Adv 5, eaaw3963, doi:10.1126/sciadv.aaw3963 (2019). [PubMed: 31355332]
74. Smucker JD & Fredericks DC Assessment of Progenix((R)) DBM putty bone substitute in a rabbit posterolateral fusion model. Iowa Orthop J 32, 54–60 (2012). [PubMed: 23576922]
75. Heijl L, Heden G, Svardstrom G & Ostgren A Enamel matrix derivative (EMDOGAIN) in the treatment of intrabony periodontal defects. J Clin Periodontol 24, 705–714, doi:10.1111/j.1600-051x.1997.tb00253.x (1997). [PubMed: 9310876]
76. Lee KY & Mooney DJ Alginate: properties and biomedical applications. Prog Polym Sci 37, 106–126, doi:10.1016/j.progpolymsci.2011.06.003 (2012). [PubMed: 22125349]
77. Lose G, Mouritsen L & Nielsen JB A new bulking agent (polyacrylamide hydrogel) for treating stress urinary incontinence in women. BJU Int 98, 100–104, doi:10.1111/j.1464-410X.2006.06205.x (2006). [PubMed: 16831152]
78. Kasi AD, Pergialiotis V, Perrea DN, Khunda A & Doumouchtsis SK Polyacrylamide hydrogel (Bulkamid(R)) for stress urinary incontinence in women: a systematic review of the literature. Int Urogynecol J 27, 367–375, doi:10.1007/s00192-015-2781-y (2016). [PubMed: 26209952]
79. Qaqish RB & Amiji MM Synthesis of a ūorescent chitosan derivative and its application for the study of chitosan±mucin interactions. Carbohydrate Polymers 38, 8 (1999).
80. Zelenski NA et al. Flexor Pollicis Longus Tendon Wear Associated With Volar Plating: A Cadaveric Study. J Hand Surg Am 46, 106–113, doi:10.1016/j.jhsa.2020.07.022 (2021). [PubMed: 32950317]
81. Carpenter AE et al. CellProfiler: image analysis software for identifying and quantifying cell phenotypes. Genome Biol 7, R100, doi:gb-2006–7-10-r100 [pii] 10.1186/gb-2006-7-10-r100 (2006). [PubMed: 17076895]

82. Shih TY et al. Injectable, Tough Alginate Cryogels as Cancer Vaccines. Adv Healthc Mater 7, e1701469, doi:10.1002/adhm.201701469 (2018). [PubMed: 29441705]
83. Pardes AM et al. Aging leads to inferior Achilles tendon mechanics and altered ankle function in rodents. In Review (2016).
84. Mienaltowski MJ, Adams SM & Birk DE Regional differences in stem cell/progenitor cell populations from the mouse achilles tendon. Tissue Eng Part A 19, 199–210, doi:10.1089/ten.TEA.2012.0182 (2013). [PubMed: 22871316]
85. Strober W Trypan blue exclusion test of cell viability. Curr Protoc Immunol Appendix 3, Appendix 3B, doi:10.1002/0471142735.ima03bs21 (2001).
86. Freedman BR, Zuskov A, Sarver JJ, Buckley MR & Soslowsky LJ Evaluating changes in tendon crimp with fatigue loading as an ex vivo structural assessment of tendon damage. J Orthop Res 33, 904–910, doi:10.1002/jor.22875 (2015). [PubMed: 25773654]
87. Peltz CD et al. The effect of postoperative passive motion on rotator cuff healing in a rat model. J Bone Joint Surg Am 91, 2421–2429, doi:10.2106/JBJS.H.01121 (2009). [PubMed: 19797578]
88. Freedman BR et al. Nonsurgical treatment and early return to activity leads to improved Achilles tendon fatigue mechanics and functional outcomes during early healing in an animal model. J Orthop Res 34, 2172–2180, doi:10.1002/jor.23253 (2016). [PubMed: 27038306]
89. Verdenius HH & Alma L A quantitative study of decalcification methods in histology. Journal of clinical pathology 11, 229–236 (1958). [PubMed: 13539226]
90. Gordon J et al. Achilles tendons from decorin- and biglycan-null mouse models have inferior mechanical and structural properties predicted by an image-based empirical damage model. Journal of Biomechanics In review (2014).
91. Gudnason K, Sigurdsson S & Jonsdottir F A Numerical Framework for Diffusive Transport in Rotational Symmetric Systems with Discontinuous Interlayer Conditions. IFAC=PapersOnLine 51, 5, doi:10.1016/j.ifacol.2018.03.109 (2018).
92. Wilke CR & Chang P Correlation of Diffusion Coefficients in Dilute Solutions. AlChE 1, 7 (1955).

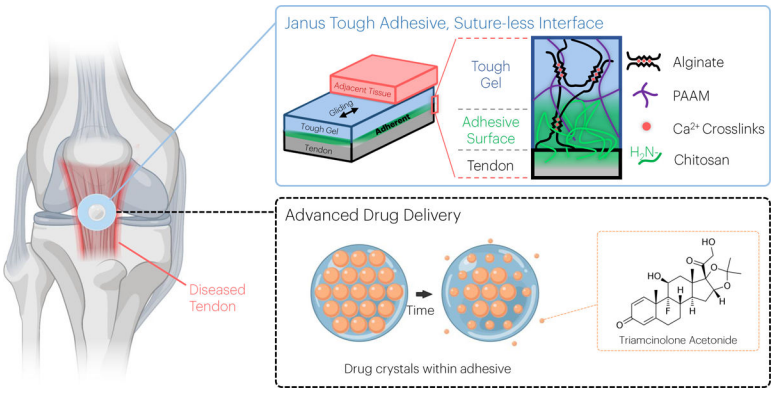

Fig. 1 |. An overview of the vision for the multifunctional performance of the Janus Tough Adhesives (JTAs) for tendon.

JTA hydrogels were engineered that comprise a tough hydrogel dissipative matrix and adhesive chitosan surface. The tough hydrogel was synthesized by combining alginate ionically crosslinked with calcium and covalently crosslinked polyacrylamide (PAAM). Beyond tissue adhesion, the material can promote gliding of surrounding tissues and serve as a drug delivery system for local release of agents such as triamcinolone acetonide as exemplified in the present study.

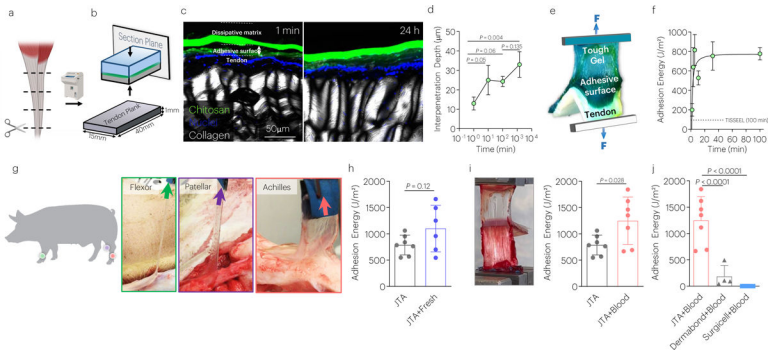

Fig. 2 |. The JTA adheres strongly to diverse tendon surfaces.

(**a**) Thin tendon planks for adhesion testing were made from bovine tendon samples using a cryotome. (**b**) The penetration of the chitosan bridging polymer into tendon in vitro was analyzed via placement of the JTA, using fluorescently labeled chitosan, on tendon planks, and quantifying chitosan depth over time. **(c)** Representative images and **(d)** quantification of penetration depth of chitosan into tendon over time. Mean values are shown and error bars represent ± s.d. (n=3 samples/group). Data were analyzed by a one-way ANOVA with post hoc t-tests with Bonferroni correction. (**e**) Peel testing was used to evaluate the adhesion energy (Blue: Tough Gel; Green: Adhesive Surface; White: tendon). (**f**) Quantification of the adhesion energy of JTA to tendon, over time, and comparison to the value achieved with TISSEEL at 100 minutes (dotted line). Mean values are shown and error bars represent ± s.d. (n=3 samples/group), (**g**) Adhesion of the JTA to wet and bloody porcine patellar, flexor carpi ulnaris, and Achilles tendons. (**h**) Porcine Achilles tendon immediately post-mortem was evaluated (JTA+Fresh) and compared to frozen tendon planks (JTA). Mean values are shown and error bars represent ± s.d. (n=6–7/group), as analyzed by a Student's t-test. (**i**) The effect of blood on JTA adhesion to tendon was evaluated. Mean values are shown and error bars represent ± s.d. (n=6–7/group), as analyzed by a Student's t-test. (**j**) Adhesion comparison of the JTA, Dermabond, and Surgicel to bloody tendons was evaluated. Mean values are shown and error bars represent ± s.d. (n=4–7 samples/group), as analyzed by a one-way ANOVA with post hoc t-tests with Bonferroni correction.

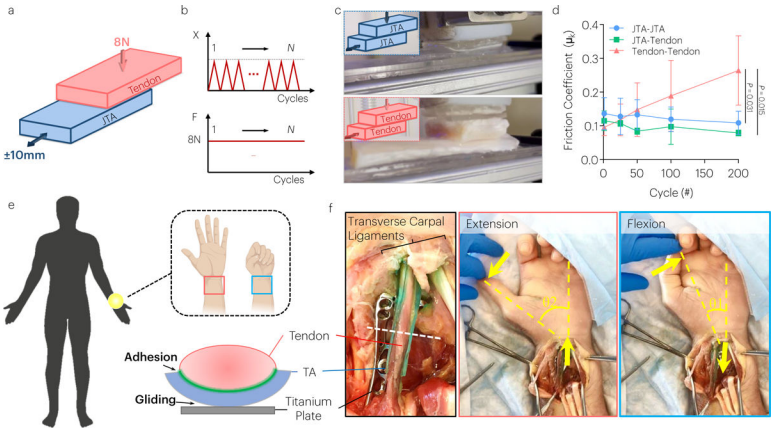

Fig. 3 |. The JTA promotes tendon gliding.

(**a,b**) To evaluate friction properties during cyclic loading, an 8N normal force was applied vertically while a lower horizontal actuator moved cyclically +/− 10 mm (2 mm/s). (**c**) Images of the cyclic friction experiments for the JTA-JTA and tendon-tendon tests. (**d**) The effect of time and group on the coefficient of kinetic friction (μ_k) was evaluated. Mean values are shown and error bars represent ± s.d. (n=3–5 samples/group), as analyzed by a two-way ANOVA with post hoc tests with Bonferroni Corrections. (**e,f**) The ability for the JTA to support gliding of the flexor digitorum profundus tendon through the transverse carpal ligaments and over volar plates was evaluated in human cadaveric limbs.

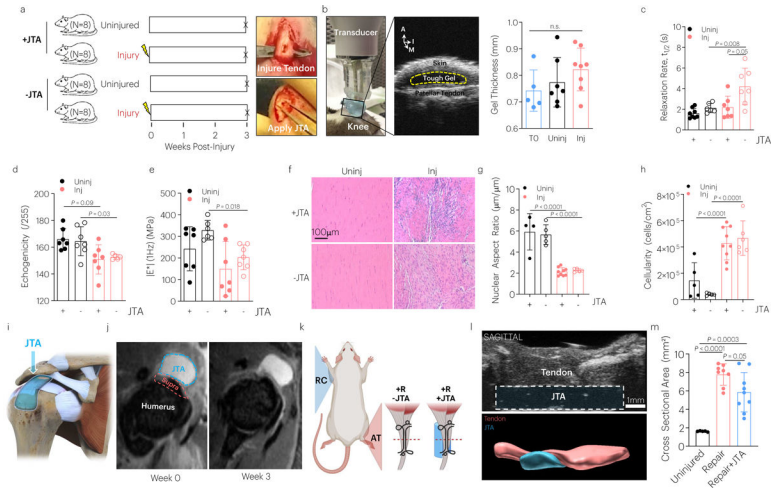

Fig. 4 |. The JTA is biocompatible to tendon and supports healing.

(**a**) The effect of patellar tendon injury and JTA implantation on tendon structural and mechanical properties was investigated. Following injury, the JTA was applied on the central midsubstance of the patellar tendon. (**b**) At 3-weeks post implantation, gel thickness was evaluated using high frequency ultrasound. Mean values are shown and error bars are ± s.d. (n=5–8 samples/group), as analyzed by a one-way ANOVA. A- Anterior; I- Inferior; M- Medial. (**c-e**) The effect of healing and JTA implantation on patellar tendon relaxation half-life, echogenicity, and |E*| was evaluated. Mean values are shown and error bars are +s.d. (n=6–8 samples/group), as analyzed by a two-way ANOVA with post hoc t-tests with Bonferroni corrections. (**f-h**) The effect of healing and JTA implantation on patellar tendon nuclear aspect ratio and cellularity was evaluated. Scale bar = 100 μm. Mean values are shown and error bars are ± s.d. (n=4–8 samples/group), as analyzed by a two-way ANOVA with post hoc t-tests with Bonferroni correction. (**i,k**) The JTA was designed to be placed over the supraspinatus tendon and pass under the acromion for testing in the rotator cuff. (**j**) T2-weighted MRI images were acquired from the rotator cuff to examine JTA placement and material compatibility over time. (**k**) The effect of the JTA on Achilles tendon healing in a repair model was evaluated. (**l**) Sagittal high frequency ultrasound imaging evaluated JTA (blue) placement over time adjacent to the Achilles tendon (red). (**m**) Axial high frequency ultrasound imaging examined the effect of tendon repair with and without the JTA on Achilles tendon cross sectional area. Mean values are shown and error bars are ± s.d. (n=8–9 tendons/group), as analyzed by a one-way ANOVA with post hoc t-tests with Bonferroni corrections.

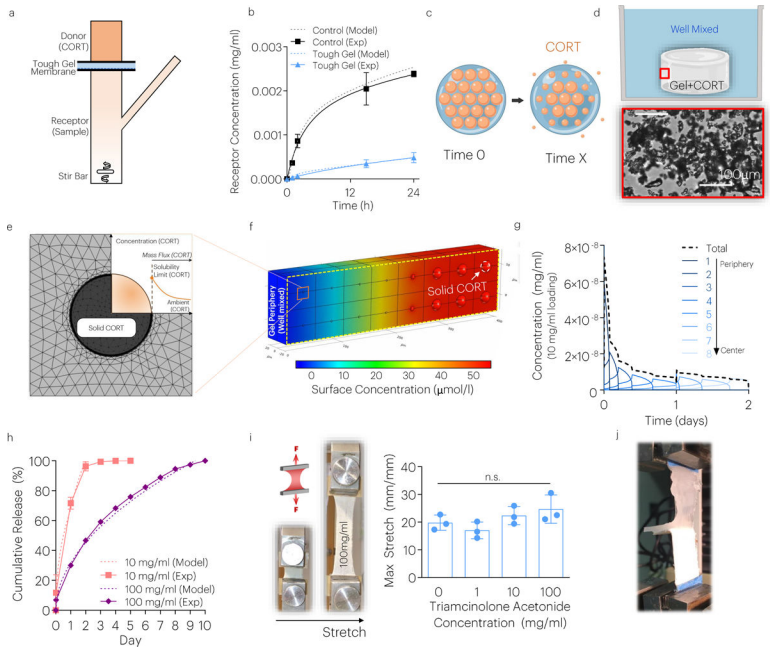

Fig. 5 |. The JTA enables dissolution-controlled release at high drug loadings.

(**a**) The CORT diffusion through the JTA was evaluated using a Franz cell. (**b**) Computational modeling and experiments evaluated the diffusion constant of the JTA. Mean values are shown and error bars are ± s.d. (n=4–6 samples/group). **(c)** In addition to diffusion-controlled release, dissolution-controlled release was investigated by loading CORT crystals (orange) within the JTA. (**d**) CORT aggregation and dissolution within the JTA was modeled based on brightfield microscopy images within pre-gel solution. (**e,f**) Dissolution of solid CORT was modeled using FE simulations under well mixed conditions to predict dissolution of particles. (**g**) Dissolution of CORT particles occurred from the gel periphery to center. (**h**) The effect of CORT loading on drug release was evaluated. Mean values are shown and error bars are ± s.d. (n=3 samples/group). (**i,j**) The effects of drug loading on JTA tensile properties and adhesion were evaluated. Mean values are shown and error bars are +s.d. (n=4 samples/group), as analyzed by a one-way ANOVA.

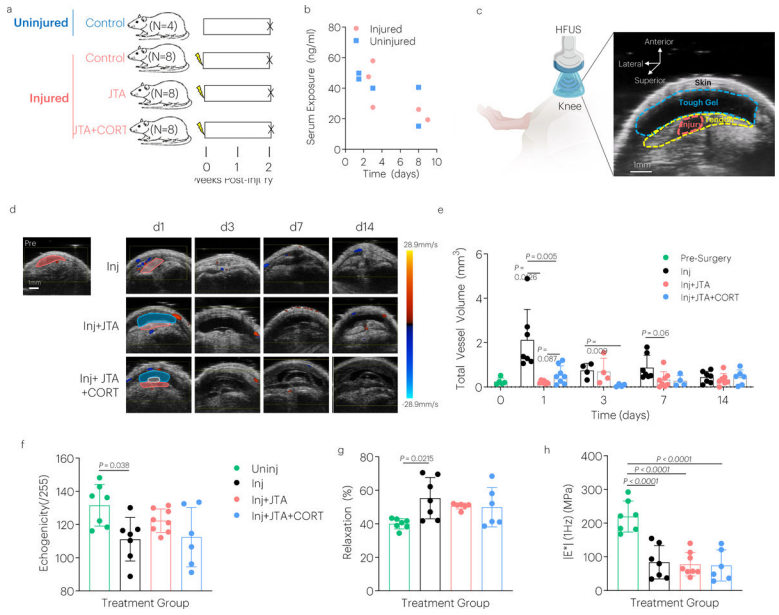

Fig. 6 |. The JTA modulates vascularization and tendon properties in a rat model of patellar tendon injury.

(**a**) The effect of the JTA loaded with triamcinolone acetonide (CORT) on patellar tendon vascularity was investigated. (**b**) CORT concentrations in serum were evaluated over time in uninjured and injured groups. (**c**) High frequency ultrasound (HFUS) imaging revealed continued adhesion of the JTAs to tendon. (**d,e**) The effect of treatment and time on total blood vessel volume after injury was evaluated using HFUS Doppler imaging. Mean values are shown and error bars are ± s.d. (n=4–7 samples/group), as analyzed by a two-way ANOVA with post hoc t-tests with Bonferroni correction. (**f,g,h**) The effect of treatment on tendon biomechanics after injury was evaluated. Mean values are shown and error bars are ± s.d (n=6–9 samples/group), as analyzed by a one-way ANOVA with post hoc t-tests with Bonferroni correction.

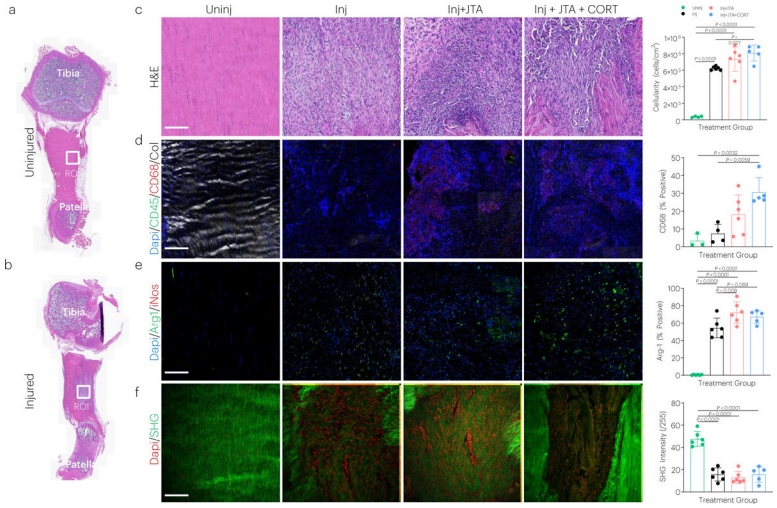

Fig. 7 |. The JTA induces immune modulation in tendon following injury.

(**a,b**) Full length histology (H&E staining) of uninjured and injured coronal tendon sections showing the region of interest (ROI) analyzed during image processing (midstance injury site) (**c-f**) Effect of injury, JTA, and JTA+CORT on tendon, as assessed by H&E (cellularity), immunostaining (CD68, Arg1), and SHG imaging (collagen signal) of tendon sections. Mean values are shown and error bars represent ± s.d. (n=5–6 samples/group), as analyzed by a one-way ANOVAs with post hoc Tukey Tests.